Multiscale Model. Simul.
Vol. 9, No. 3, pp. 1144–1161

COHERENT VORTICITY SIMULATION OF THREE-DIMENSIONAL FORCED HOMOGENEOUS ISOTROPIC TURBULENCE*

NAOYA OKAMOTO[†‖], KATSUNORI YOSHIMATSU[‡], KAI SCHNEIDER[§], MARIE FARGE[¶], AND YUKIO KANEDA[‡]

Abstract. Coherent vorticity simulation (CVS) is a multiscale method to compute incompressible turbulent flows based on the wavelet filtered Navier–Stokes equations. At each time step the vorticity field is decomposed into two orthogonal components using an orthogonal wavelet basis: the coherent vorticity, corresponding to the coefficients whose modulus is larger than a threshold, and the remaining incoherent vorticity. The threshold value only depends on the total enstrophy, which evolves in time, and on the maximal resolution, which remains constant. The induced coherent velocity is computed from the coherent vorticity using the Biot–Savart kernel. To compute the flow evolution one only retains the coherent wavelet coefficients and some of their neighbors in space, scale, and direction, which define the safety zone. Two different strategies are studied to minimize at each time step the number of degrees of freedom to be computed, either by increasing the threshold value or by reducing the width of the safety zone. Their efficiency is compared for a three-dimensional forced homogeneous isotropic turbulent flow at initial Taylor microscale Reynolds number $R_\lambda = 153$. The quality of the results is assessed in comparison to a direct numerical simulation of the same flow. It is found that, as long as a safety zone is present, CVS well preserves the statistical predictability of the turbulent flow (even the vorticity and velocity probability distribution functions) with a reduced number of degrees of freedom.

Key words. wavelets, turbulence modeling, homogeneous turbulence, coherent structures

AMS subject classifications. 76F05, 76F65, 65T60

DOI. 10.1137/10079598X

1. Introduction.

Turbulence, ubiquitous in our daily life, is still one of the most challenging problems in science. Turbulence exhibits an intrinsic multiscale behavior due to a large number of degrees of freedom interacting nonlinearly. Observations show its self-organization into vortices, even at large Reynolds' number [3], superimposed to a background flow. This motivates us to split turbulent flows into two contributions, i.e., coherent vortices and a random background flow. Both contributions are multiscale and exhibit no scale separation. To reduce the computational load for simulating turbulent flow we have proposed the coherent vorticity simulation (CVS) method, which retains only the flow induced by the coherent vortices [7], [8]. This approach differs from the filtering approach of large-eddy simulation (LES), e.g., [15], [18], which computes only the large-scale evolution, while modeling the influence of small-scale motion onto the

*Received by the editors May 20, 2010; accepted for publication (in revised form) May 5, 2011; published electronically September 1, 2011. This work was supported by the Grant-in-Aids for Scientific Research (B) 20340099 from the Japan Society for the Promotion of Science (JSPS), Young Scientists(B) 20760055 and Young Scientists(B) 22760063 from the Ministry of Education, Culture, Sports, Science and Technology.
http://www.siam.org/journals/mms/9-3/79598.html

[†]Center for Computational Science, Graduate School of Engineering, Nagoya University, Nagoya 464-8603, Japan (okamoto@ccs.engg.nagoya-u.ac.jp).

[‖]JST, CREST, 5, Sanbancho, Chiyoda, Tokyo 102-0075, Japan.

[‡]Department of Computational Science and Engineering, Nagoya University, Nagoya 464-8603, Japan (yosimatu@fluid.cse.nagoya-u.ac.jp, kaneda@cse.nagoya-u.ac.jp).

[§]M2P2-CNRS and Centre de Mathématiques et d'Informatique, Université de Provence, 39 rue Frédéric Joliot–Curie, 13453 Marseille Cedex 13, France (kschneid@cmi.univ-mrs.fr). This author's research was supported by the Agence Nationale de la Recherche, project "M2TFP," and by Association CEA-Euratom.

[¶]LMD-IPSL-CNRS, Ecole Normale Supérieure, 24 rue Lhomond, 75231 Paris Cedex 05, France (farge@lmd.ens.fr).This author's research was supported by the Agence Nationale de la Recherche, project "M2TFP," and by Association CEA-Euratom.

large-scale motion. In laboratory experiments and in direct numerical simulation (DNS) one observes that small-scale contributions are not necessarily slaved by the large scales since there is some inverse energy transfer, called backscattering, which complicates modeling in LES.

So far different multiscale decompositions have been applied for modeling and computing turbulent flows [6], [11], [17], [22]. The wavelet representation is an efficient tool to perform such decompositions since it uses well localized functions in space, scale, and direction. It has been utilized to extract coherent vorticity with a reduced set of degrees of freedom from two- [7] and three-dimensional incompressible hydrodynamic turbulence [9], [10] to extract coherent vorticity sheets and current density sheets from magnetohydrodynamic turbulence [30] and also to perform directional statistical analyses [2]. Okamoto et al. [20] have shown that for three-dimensional homogeneous isotropic turbulence, the number of degrees of freedom N_c of the coherent vorticity increases more slowly with the Taylor microscale Reynolds number R_λ, i.e., $N_c \propto R_\lambda^{3.9}$, than the number of degrees of freedom of DNS N, where Kolmogorov type arguments imply $N \propto R_\lambda^{9/2}$. One might think that the improvement of the scaling exponent is small. However, the coefficient in front was shown to be about a factor 10 smaller than that of DNS, which implies a significant reduction, i.e., a reduction of one order of magnitude of the number of degrees of freedom in CVS.

The CVS approach was originally introduced in [7], [8]. The underlying idea of CVS is to decompose the turbulent flow at each time step into organized coherent and noise-like incoherent contributions using an orthogonal wavelet representation of vorticity. The coherent vorticity is reconstructed from the few wavelet coefficients whose modulus is larger than a given threshold, while the incoherent vorticity is obtained from the many remaining wavelet coefficients. Only the coherent flow is computed deterministically, while the incoherent flow is discarded or statistically modeled. The choice of the threshold, which is applied to the wavelet coefficients, is directly related to Donoho's criterion [5], and hence its value is determined automatically during the flow evolution. This criterion supposes the incoherent flow to be Gaussian and decorrelated. Different examples of CVS for two-dimensional turbulent flows can be found in [7], [8], [12], [25] and for three-dimensional turbulent mixing layers in [24]. In [12], [24], [25], a safety zone in wavelet space was introduced in order to predict the translation of coherent vorticity and the generation of smaller scales due to its nonlinear dynamics.

CVS-like computations of three-dimensional homogeneous isotropic decaying and forced turbulence and its coupling with LES are presented in [13], [27]. In these CVS-like simulations, the velocity is decomposed into biorthogonal wavelets, and the coherent velocity is advanced in time using an adaptive wavelet collocation method with a finite difference discretization. The threshold there is determined a priori from DNS results. The resolution of the CVS-like computations was increased by a factor of 8 with respect to DNS as, instead of a Fourier spectral method, a finite difference scheme is used. Readers interested in wavelet methods in computational fluid dynamics may refer to the recent review article [26].

The aim of the present work is to assess the potential of CVS for three-dimensional forced homogeneous isotropic turbulence. The choice of homogeneous turbulence is made to demonstrate the feasibility and efficiency of CVS by choosing the most challenging case. Indeed, in homogeneous turbulence, coherent vortices are spread all over physical space, in contrast to inhomogeneous turbulence, e.g., mixing layers or flows past bluff bodies. The motivation to analyze forced turbulence is to obtain a statistically stationary flow and to keep the small scales active.

We investigate the choice of the safety zone and of the threshold, as they play a significant role regarding CVS efficiency and reliability. The CVS results are compared to DNS results using the same maximal resolution and also to Fourier truncated simulation using the spectral cutoff filter. Thus, we check if we can benefit from the wavelet representation with respect to the predictability of turbulence in the statistical sense, and not in the determinisitc sense as the system is chaotic. In the present study, we perform CVS using pseudoadaptive computations in the same way as in [24] to check the feasibility of fully adaptive computations, and therefore we do not focus on the CPU time of CVS. Fully adaptive CVS computations of three-dimensional turbulent flows will reduce not only the memory requirements but also the CPU time of the computations, as shown for three-dimensional weakly compressible mixing layers using an adaptive multiresolution method [21].

The remainder of the paper is organized as follows. First, the CVS methodology is exposed in section 2, and then different choices of the safety zone are discussed in section 3. Section 4 presents numerical results, and finally section 5 gives conclusions and perspectives.

2. CVS methodology. In this section, we describe the CVS methodology, i.e., the coherent vorticity extraction (CVE) method, the wavelet filtered Navier–Stokes equations, and safety zones.

2.1. Coherent vorticity extraction. We briefly summarize the CVE method for three-dimensional turbulent flows, which was first introduced in [9]. This approach is based on a decomposition of vorticity $\boldsymbol{\omega} = \nabla \times \boldsymbol{u}$ into an orthogonal discrete wavelet series, i.e.,

$$\boldsymbol{\omega}(\boldsymbol{x}) = \sum_{\lambda \in \Lambda} \tilde{\boldsymbol{\omega}}_\lambda \psi_\lambda(\boldsymbol{x}), \tag{2.1}$$

where the multi-index $\lambda = (j, i_1, i_2, i_3, \mu)$ denotes the scale 2^{-j}, the position $2^{-j}\boldsymbol{i} = 2^{-j}(i_1, i_2, i_3)$, and the seven directions $\mu = 1, \ldots, 7$ of the wavelets. The index set of the wavelet coefficients Λ is

$$\Lambda = \{\lambda = (j, i_n, \mu), j = 0, \ldots, J-1, i_n = 0, \ldots, 2^j - 1, n = 1, 2, 3, \text{ and } \mu = 1, \ldots, 7\}.$$

The discrete wavelet basis $\psi_\lambda(\boldsymbol{x})$ consists of a discrete set of continuous functions, whose index set Λ is discrete. The three-dimensional wavelets $\psi_\lambda(\boldsymbol{x})$ correspond to products of one-dimensional scaling functions and wavelets in various combinations, as shown in (Mallat, p. 340 of [16] and Meyer, p. 81 of [19]) and (Meneveau, p. 478 of [17]) for two- and three-dimensional wavelets, respectively. An illustration of the three-dimensional wavelet space is given in Figure 2.1 and the seven directions are shown in Figure 2.2(c). It can be observed that there are more coefficients as scale decreases.

Owing to orthogonality the wavelet coefficients are given by $\tilde{\boldsymbol{\omega}}_\lambda = \langle \boldsymbol{\omega}, \psi_\lambda \rangle$, where $\langle \cdot, \cdot \rangle$ denotes the L^2-inner product, defined by $\langle f, g \rangle = \int_{\boldsymbol{R}^3} f(\boldsymbol{x}) g(\boldsymbol{x}) d\boldsymbol{x}$. The coefficients measure the fluctuations of $\boldsymbol{\omega}$ around scale 2^{-j} and around position $2^{-j}\boldsymbol{i}$ for each of the seven directions. The N wavelet coefficients $\tilde{\boldsymbol{\omega}}_\lambda$ are efficiently computed from the $N = 2^{3J}$ grid point values of $\boldsymbol{\omega}$ using the fast wavelet transform which has linear computational complexity (see, e.g., [16]). In the present work, the compactly supported Coiflet wavelets with filter width 12 are used.

Thresholding the wavelet coefficients $\tilde{\boldsymbol{\omega}}_\lambda$ at a given time instant, with a thresholding function

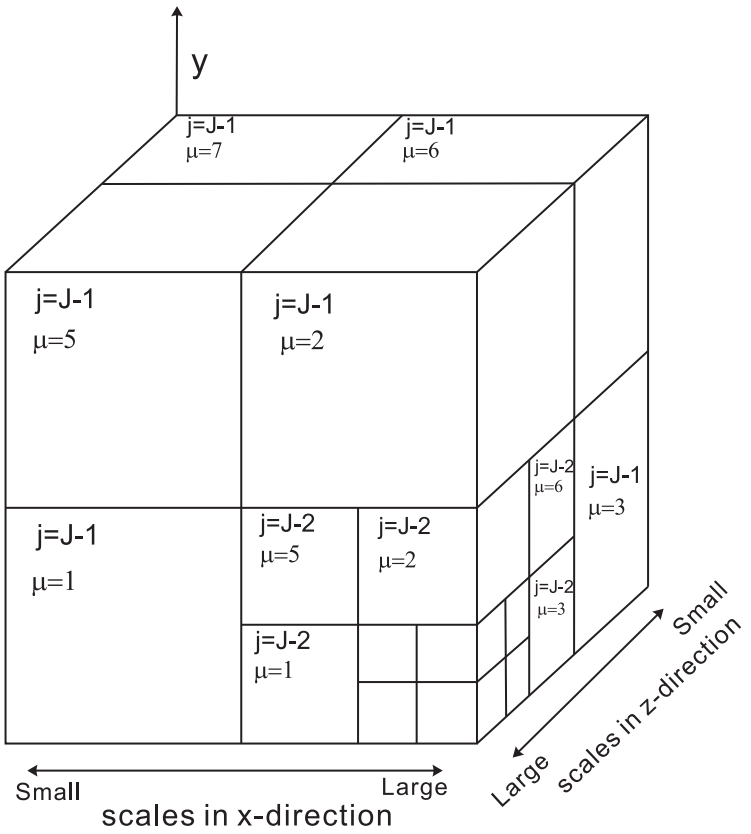

FIG. 2.1. *The orthogonal wavelet representation of a three-dimensional field. Generalizing Mallat's convention used for two-dimensional images* [16]*, each three-dimensional subcube corresponds to a given scale indexed by* j *and a given direction indexed by* μ*, all three depending on the three spatial directions* x*,* y*, and* z*.*

$$\rho_T(\tilde{\boldsymbol{\omega}}_\lambda) = \begin{cases} \tilde{\boldsymbol{\omega}}_\lambda & \text{for } |\tilde{\boldsymbol{\omega}}_\lambda| > T, \\ 0 & \text{for } |\tilde{\boldsymbol{\omega}}_\lambda| \le T, \end{cases} \tag{2.2}$$

we separate the coefficients into coherent and incoherent, i.e., $\tilde{\boldsymbol{\omega}}_c = \rho_T(\tilde{\boldsymbol{\omega}}_\lambda)$ and $\tilde{\boldsymbol{\omega}}_i = \tilde{\boldsymbol{\omega}}_\lambda - \tilde{\boldsymbol{\omega}}_c$, respectively. The coherent and incoherent vorticity fields are then reconstructed by the inverse wavelet transform. By construction we have

$$\boldsymbol{\omega} = \boldsymbol{\omega}_c + \boldsymbol{\omega}_i, \tag{2.3}$$

and, thanks to the orthogonality of the decomposition, enstrophy $Z = \langle \boldsymbol{\omega}, \boldsymbol{\omega} \rangle / 2$ is conserved, i.e., $Z = Z_c + Z_i$.

The threshold is motivated by denoising theory [5]. The threshold value is given by $T = \{(4/3) Z_i \ln N\}^{1/2}$, which depends only on the incoherent enstrophy Z_i (which is a priori unknown) and the maximal resolution N. Owing to Parseval's identity, the enstrophy can be computed directly in wavelet space. We compute the first threshold value T_0 using the total enstrophy Z as a first estimate of Z_i, i.e., $T_0 = \{(4/3) Z \ln N\}^{1/2}$. Then we split the total vorticity field $\boldsymbol{\omega}$ into coherent and incoherent vorticity with threshold $T = T_0$. The obtained incoherent enstrophy provides a new estimate of Z_i from which we compute a new threshold value T_1. The above procedure could then

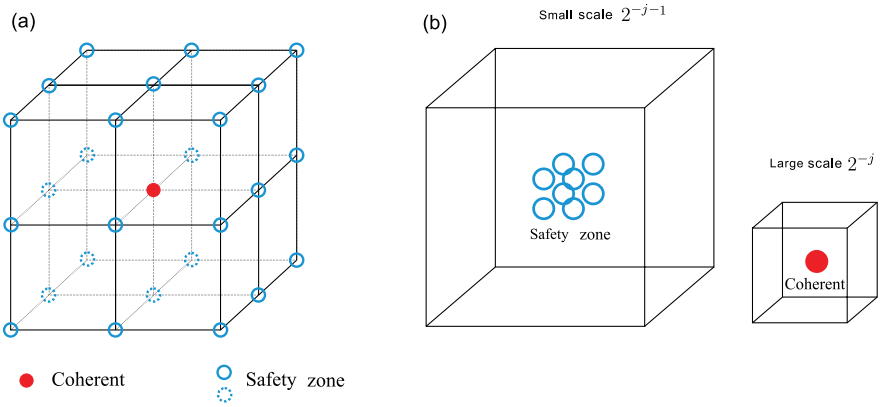

Coherent	Safety zone
μ=1	μ=4, 5
μ=2	μ=5, 6
μ=3	μ=4, 6
μ=4	μ=1, 3, 7
μ=5	μ=1, 2, 7
μ=6	μ=2, 3, 7
μ=7	μ=4, 5, 6

FIG. 2.2. *The different options for the safety zone showing the neighbors in space, scale, or direction of a given wavelet coefficient* $\tilde{\boldsymbol{\omega}}_\lambda$ *:* (a) *spatial position of the neighbor wavelet coefficients at the same scale* 2^{-j}*, and* (b) *spatial position of the neighbor wavelet coefficients at the next smaller scale* 2^{j-1}*,* (c) *directions of the neighbor wavelet coefficients.*

be iterated until convergence. For details on this iterative algorithm and its mathematical justification, we refer to [1]. The coherent vorticity extracted by wavelet filtering with $T = T_1$ is sufficient to preserve the statistics of the total field at a given time instant and achieves good compression. In contrast, the coherent vorticity field extracted by the wavelet filtering with $T = T_0 (> T_1)$ does not sufficiently preserve the statistics of the total field well [25]. The influence of the number of iterations for two- and three-dimensional homogeneous isotropic turbulence is reported in [25] and [20], respectively.

The corresponding induced velocity fields are reconstructed by applying the Biot–Savart kernel to both the coherent and incoherent vorticity fields, i.e., $\boldsymbol{u} = -\nabla \times (\nabla^{-2}\boldsymbol{\omega})$ to obtain

$$\boldsymbol{u} = \boldsymbol{u}_c + \boldsymbol{u}_i. \tag{2.4}$$

For the energy, we have $E = E_c + E_i + \varepsilon$, where $E = \langle \boldsymbol{u}, \boldsymbol{u} \rangle / 2$ and $\varepsilon / E \ll 1$. Farge, Pellegrino, and Schneider [9] showed that the incoherent velocity field is Gaussian-like and exhibits an energy equipartition.

The projection of the vorticity field onto a finite-dimensional subspace, see (2.1) in the case of wavelets (with $N = 2^J$) or the space of trigonometric polynomials of degree smaller or equal $N/2$ in the case of the Fourier tranform, yields a one-to-one correspondence between the discrete wavelet or Fourier coefficients and the continuous

functions. Thus, one can work either with the projected functions or with the coefficients. The coefficients are used in a Galerkin projection of the Navier–Stokes equations onto a finite-dimensional subspace.

2.2. Wavelet filtered Navier–Stokes equation. To track the nonlinear flow dynamics in space, scale, and direction, the CVE method should be applied at each time step. But retaining the coherent wavelet coefficients only is not sufficient to catch the flow evolution. Adding a safety zone in the vicinity of the retained wavelet coefficients is crucial, as shown in [25] for two-dimensional turbulence. The CVS method should thus retain both the coherent wavelet coefficients and their neighbor coefficients at each time step. The coherent vorticity field, including the safety zone $\boldsymbol{\omega}_{c*}$, is obtained from these wavelet coefficients, and the remaining vorticity field $\boldsymbol{\omega}_{i*}$ is $\boldsymbol{\omega}_{i*} = \boldsymbol{\omega} - \boldsymbol{\omega}_{c*}$. The corresponding velocity fields $\boldsymbol{u}_{c*}$ and $\boldsymbol{u}_{i*}$ induced by $\boldsymbol{\omega}_{c*}$ and $\boldsymbol{\omega}_{i*}$, respectively, are computed from the Biot–Savart relation. In CVS, $\boldsymbol{\omega}_{c*}$ is not perfectly divergence-free, but this is ensured by taking the curl of $\boldsymbol{u}_{c*}$. A discussion on the divergence of $\boldsymbol{\omega}_{c*}$ is given in Appendix A.

Inserting the decompositions $\boldsymbol{\omega} = \boldsymbol{\omega}_{c*} + \boldsymbol{\omega}_{i*}$ and $\boldsymbol{u} = \boldsymbol{u}_{c*} + \boldsymbol{u}_{i*}$ into the Navier–Stokes equations and neglecting the influence of $\boldsymbol{\omega}_{i*}$ and $\boldsymbol{u}_{i*}$, we obtain the evolution equation for $\boldsymbol{\omega}_{c*}$,

$$\frac{\partial}{\partial t}\boldsymbol{\omega}_{c*} + \boldsymbol{u}_{c*} \cdot \nabla \boldsymbol{\omega}_{c*} = \boldsymbol{\omega}_{c*} \cdot \nabla \boldsymbol{u}_{c*} + \nu \nabla^2 \boldsymbol{\omega}_{c*} + \nabla \times \boldsymbol{f}, \tag{2.5}$$

where ν denotes the kinematic viscosity and with $\nabla \cdot \boldsymbol{u}_{c*} = 0$. The term $\boldsymbol{f}$ expresses a solenoidal external force applied to the velocity field. The evolution of $\boldsymbol{u}_{c*}$ can be obtained by the velocity-pressure formulation, which is equivalent to (2.5) supposing the incompressibility of $\boldsymbol{\omega}_{c*}$.

2.3. Safety zone in wavelet space. The index set of the coherent wavelet coefficients at a given time instant Λ_c^n is expanded by adding the neighbor wavelets in scale, space, and direction, which corresponds to the safety zone, as illustrated in Figure 2.2. The expanded index set, denoted by Λ_*^n, thus allows one to track the translation of coherent vortices and the production of finer scales due to their nonlinear interaction. A flowchart of the CVS algorithm is shown in Figure 2.3.

As illustrated in Figures 2.2(a)–(c) the total number of neighbors is large, i.e., we have 26 adjacent neighbors in space, 2 or 3 in direction, and 8 in scale for a given coefficient. Adding all neighbors whose indices do not belong to Λ_c^n to the safety zone would significantly increase the percentage of the wavelet coefficients retained by CVS. Here we keep the incoherent wavelet coefficients belonging to the safety zone, i.e., the difference set $\Lambda_*^n - \Lambda_c^n$, at any time in order to take advantage of the safety zone as much as possible. The remaining large majority of the wavelet coefficients, which are not elements of Λ_*^n, are neglected.

The width of the safety zone depends on the time increment and on the fact that the nonlinear term is quadratic. The fluid incompressibility implies that local changes in the flow could become global. However, the wavelet representation of the flow, which uses functions with vanishing moments, implies that the energy and enstrophy transfer become local in wavelet space, as shown in Schneider et al. [24] and Fröhlich and Schneider [12] for three- and two-dimensional flows, respectively. These studies suggest that the information which travels further than the adjacent wavelet coefficients is not significant, given that the time increment is sufficiently small. However, one should verify whether the width of the safety zone is sufficient to preserve the flow dynamics well.

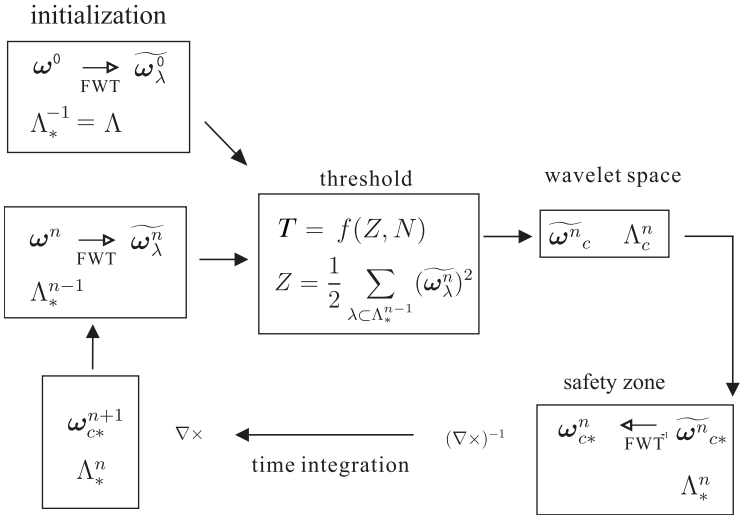

FIG. 2.3. *Flowchart of CVS.*

3. Numerical method and simulation settings. The numerical code uses a classical Fourier pseudospectral method based on the velocity-pressure formulation with a fourth-order Runge–Kutta scheme for time marching. We compute in each time step the vorticity field, perform the wavelet filtering of vorticity including the definition of the safety zone in order to obtain the coherent vorticity, and invert the curl operator to compute the coherent velocity field, which is advanced in time (see Figure 2.3). The aliasing errors are removed by a phase-shift method, which keeps all the Fourier modes satisfying $k = |\boldsymbol{k}| < k_{\max}$, where $\boldsymbol{k}$ is the wave vector and $k_{\max} = 2^{1/2} N^{1/3}/3$.

The external force $\mathcal{F}[\boldsymbol{f}](\boldsymbol{k}, t)$ is applied to $\mathcal{F}[\boldsymbol{u}](\boldsymbol{k}, t)$ in the low wavenumber range $k < 2.5$, where $\mathcal{F}[\cdot]$ denotes the Fourier representation of $\cdot$. The force satisfies the following conditions:

$$\langle \mathcal{F}[f_\ell](\boldsymbol{k}, t) \rangle = 0, \tag{3.1}$$

$$\langle \mathcal{F}[f_\ell](\boldsymbol{k}, t+\tau) \mathcal{F}[f_m](-\boldsymbol{k}', t) \rangle = F \left(\delta_{\ell m} - \frac{k_\ell k_m}{k^2} \right) \delta_{\boldsymbol{k},\boldsymbol{k}'} e^{-|\tau|/\tau_c}, \tag{3.2}$$

where f_ℓ is the ℓth component of $\boldsymbol{f}$, F the intensity of $\boldsymbol{f}$, τ_c the correlation time of the external force, $\delta_{\ell m}$ the Kronecker delta $\delta_{\boldsymbol{k},\boldsymbol{k}'} = 1$ for $\boldsymbol{k} = \boldsymbol{k}'$, and $\delta_{\boldsymbol{k},\boldsymbol{k}'} = 0$ else. The bracket $\langle\rangle$ denotes the ensemble average. Readers interested in details of how to generate such a random force are referred to the appendix of [29].

We performed eight numerical computations of forced homogeneous isotropic turbulence in a 2π periodic box: one DNS computation as reference, five CVS computations (CVS0, CVS1, CVS2, CVS3, and CVS4), and two Fourier truncated simulations (FL0 and FL1) using the spectral cutoff filter. The different CVS computations are summarized in Table 3.1. The safety zones in CVS0 and CVS1 are determined in the same way as in [8], [12], [24], [25]. The resolution is $N = 256^3$, the kinematic viscosity $\nu = 7.0 \times 10^{-4}$, and the time increment $\Delta t = 1.0 \times 10^{-3}$. The external force has the same time history in all the above computations. Here we set $\tau_c = 0.5$ and $F = 1.5 \times 10^{-3}$.

TABLE 3.1
Safety zone and threshold used for CVS (∘ for active safety zone, × for nonactive safety zone).

	safety zone			
	space	direction	scale	threshold value T
CVS0	∘	∘	∘	T_0
CVS1	∘	∘	∘	T_1
CVS2	∘	∘	×	T_1
CVS3	×	×	∘	T_1
CVS4	×	×	×	T_1

TABLE 3.2
Physical parameters of the DNS, CVS, and FL computations at $t/\tau = 3.78$.

	E	$E/E_{\mathrm{DNS}}(\%)$	Z	$Z/Z_{\mathrm{DNS}}(\%)$	L	λ	η	$-S_u$	$F_{\boldsymbol{\omega}}$
DNS	0.516	100	71.4	100	0.942	0.190	0.00765	0.491	7.99
CVS 0	0.529	103	45.8	64.1	0.893	0.240	0.00855	0.494	8.41
CVS 1	0.514	99.6	56.6	79.3	0.945	0.213	0.00811	0.511	8.72
CVS 2	0.512	99.2	51.1	71.6	0.898	0.224	0.00832	0.475	7.19
CVS 3	0.518	100	55.0	77.0	0.915	0.217	0.00817	0.509	8.80
CVS 4	0.534	103	14.1	19.7	0.997	0.436	0.01149	0.394	4.60
FL 1	0.518	100	71.4	100	0.939	0.190	0.00765	0.465	7.30
FL 0	0.520	101	72.1	101	0.942	0.190	0.00763	0.377	5.70

All the above computations are integrated during about four initial eddy turnover times $\tau = L/u'^2$, where $u' = 2E/3$ and L is the integral length scale defined by $L = \pi/(2u'^2)\int_0^{k_{\max}} E(k)/k\mathrm{d}k$. Here, $E(k)$ is the energy spectrum, defined as $E(k) = \Sigma_{k-1/2\le|\boldsymbol{p}|<k+1/2}|\mathcal{F}[\boldsymbol{u}](\boldsymbol{p})|^2/2$. The Kolmogorov length scale η is defined by $\eta = (\nu^3/\langle\epsilon\rangle)^{1/4}$, where $\langle\epsilon\rangle$ is the mean rate of energy dissipation per unit mass. Typical physical quantities are summarized in Table 3.2.

We use the same initial velocity field in all the computations. This initial flow field is obtained by a preceding DNS computation of a statistically quasi-steady turbulent flow with a Taylor microscale Reynolds number $R_\lambda = 153$. Here, $R_\lambda = u'\lambda/\nu$, λ is the Taylor microscale length defined by $\lambda = (15\nu u'^2/\langle\epsilon\rangle)^{1/2}$. The initial energy spectrum of the DNS has the form $E(k) \propto k^4 \exp(-2k^2/k_p^2)$. Here, $k_p = 2$ and the initial total energy is 0.5.

The numerical procedure to simulate CVS using a Fourier solver is close to real adaptive CVS computations, as the concept of the safety zone is completely identical. However, we should keep in mind that in our case the flow is computed in a Fourier basis. Thus, derivation and integration are exact in Fourier space, which is not the case in a wavelet basis. An exception are Shannon wavelets, which are made out of trigonometric polynomials. For Shannon wavelets, the adaptive CVS computation would be algebraically identical to the Fourier solver. For other wavelet bases, e.g., spline wavelets, the difference between the wavelet and Fourier schemes becomes smaller with increasing order of the wavelet. Readers interested in the estimation of numerical cost of fully adaptive CVS are referred to Appendix B.

4. Numerical results. In this section, we study the choice of the safety zone and then examine the dependence of CVS on the threshold. Finally, we compare CVS with Fourier truncated simulations.

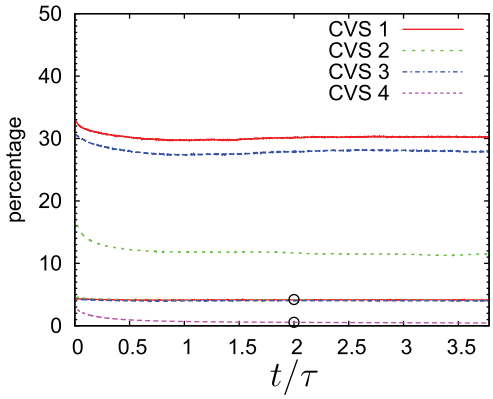

FIG. 4.1. *Time evolution of the percentage of retained wavelet coefficients with and without safety zone for CVS*1–4*. The curve for the percentage without safety zone, marked with* ∘*, superimposes well for CVS*1–3*, while the curve for CVS*4 *is below those for CVS*1–3*.*

4.1. Influence of the safety zone. Figure 4.1 shows the time evolution of the percentage of retained coefficients in CVS. They consist of the coherent wavelet coefficients and the wavelet coefficients retained in the safety zone. In each case, we see that after a transient decay at early times, say $t > 0.5\tau$, the number of the retained coefficients does not vary much. Most coefficients are retained by CVS1 (about 30%), followed by CVS3 (about 27%), and then CVS2 (11.5%). For CVS4, where no safety zone is present, the number of retained wavelet coefficients decays rapidly below 0.5%.

Flow visualizations of intense vorticity regions for CVS1, CVS2, and CVS3 (abbreviated as CVS1–3 here) and the reference DNS show a statistically similar picture of turbulent vorticity which consists of entangled vortex tubes (see Figure 4.2). From a deterministic point of view, the instantaneous flow fields do not exactly coincide due to the sensitivity to initial conditions of any flows as soon as they reach the turbulent regime. This is consistent with the results in [28], which showed that turbulent flow is sensitive to the resolution level $k_{\max}\eta$ even if $k_{\max}\eta \gtrsim 1$. From the visualization of CVS4, we see that the dynamics is lost as the vorticity structure is no longer preserved because no safety zone has been added in this case.

In Figure 4.3(left), the ratio of energy for CVS to that for DNS is plotted as a function of time. For the ratio, we see reasonable agreement for CVS1–3: the time evolutions of CVS1–3 differ from the evolution of DNS by less than only 1.5%, while the time evolution of CVS4 differs by at most 8%.

CVS1–3 retain between 62% and 82% of the DNS enstrophy for $t > 0.5\tau$, as shown in Figure 4.3(right). We also observe that the best result is obtained for CVS1, where the safety zone is taken in space, scale, and direction and where the retained enstrophy varies between 75% and 82%. For CVS4, the enstrophy rapidly decays and retains only 20% enstrophy of DNS for $t > 0.5\tau$.

To get insight into the spectral distribution of energy, we plot the energy spectra $E(k)$ for the different runs in Figure 4.4(left). We find that CVS1–3 again agree well with the DNS in terms of $E(k)$. Although the energy spectra for CVS1–3 are different from the spectrum of DNS in the dissipative range, i.e., $k\eta \gtrsim 0.3$, they still have significant contributions in the dissipative range. The energy flux $\Pi(k)$ in Figure 4.4(right) confirms that all the nonlinear dynamics are well retained in CVS1–3, where $T(k)$ and

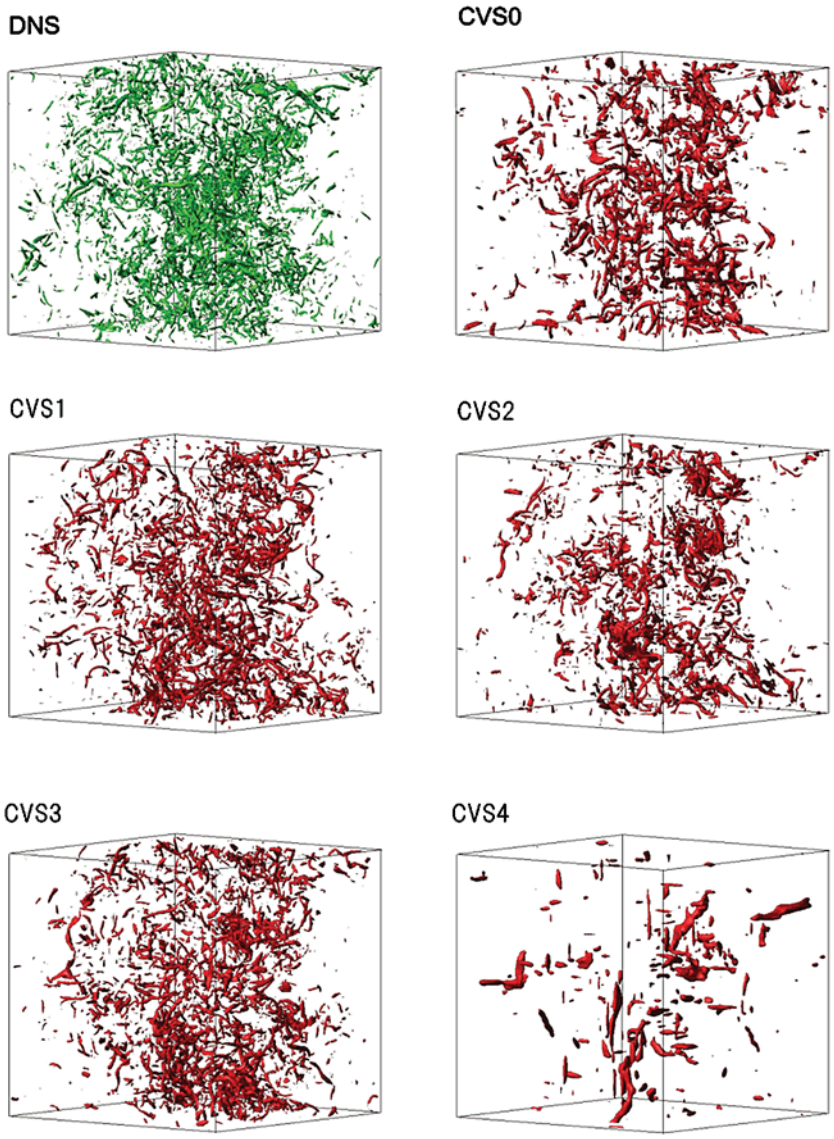

FIG. 4.2. *Visualization of the intense vorticity regions for DNS (in green) and (CVS0–4) (in red) at* $t/\tau = 3.78$. *Isosurfaces of vorticity are shown for* $|\boldsymbol{\omega}| = M + 4\sigma$, *where* M *and* σ *denote the mean value and standard deviation of the modulus of each vorticity field. (Corresponding movies can be downloaded from http://ccs.engg.nagoya-u.ac.jp/CVS/HIT_forced/)*

$\Pi(k)$ are defined by $T(k) = -\sum_{k-1/2\le|\boldsymbol{p}|<k+1/2}\mathcal{F}[\boldsymbol{u}](-\boldsymbol{p})\cdot\mathcal{F}[(\boldsymbol{u}\cdot\nabla)\boldsymbol{u}](\boldsymbol{p})$ and $\Pi(k) = -\int_0^k T(k)\mathrm{d}k$, respectively.

The skewness of the longitudinal velocity derivative $\partial u/\partial x$, defined by $S_u = \langle(\partial u/\partial x)^3\rangle/\langle(\partial u/\partial x)^2\rangle^{3/2}$ (Figure 4.5, left), and the flatness of vorticity, defined by $F_\omega = \langle\omega_\ell^4\rangle/\langle\omega_\ell^2\rangle^2$ (Figure 4.5, right), yield information on higher order statistics of the flow. For the time evolution of the former, we find similar tendencies for CVS1–3. CVS1–3 exhibit almost constant values which are close to the DNS value. For the latter, we see that the values of the vorticity flatness for CVS1 and CVS3 remain close to each other and above the value for DNS. These larger flatness values quantify that the

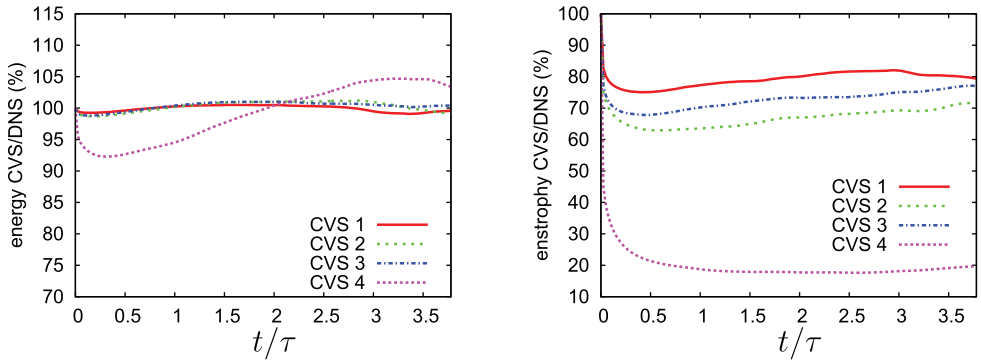

FIG. 4.3. *Left: The ratio of energy between CVS and DNS. Right: The ratio of enstrophy between CVS and DNS.*

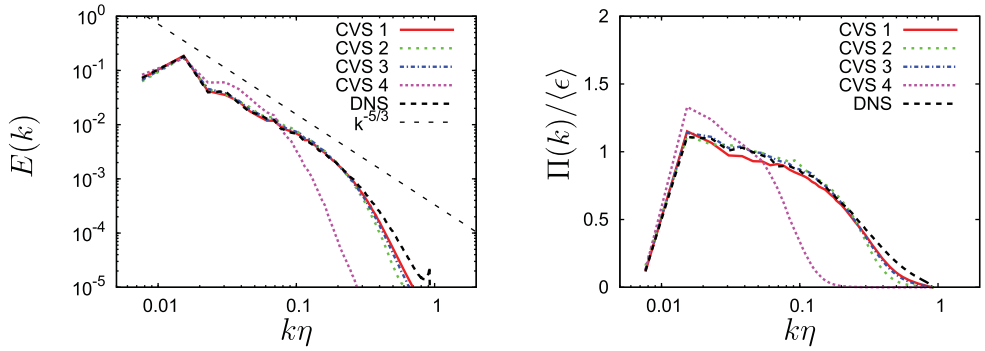

FIG. 4.4. *Energy spectra $E(k)$ (left) and energy fluxes $\Pi(k)$ (right) at $t/\tau = 3.78$. The wavenumber k and the flux $\Pi(k)$ are respectively normalized by η and $\langle\epsilon\rangle$ of the DNS at $t/\tau = 3.78$.*

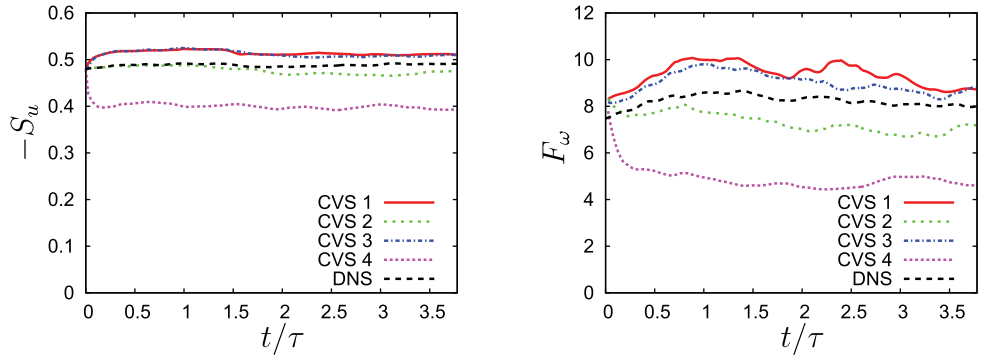

FIG. 4.5. *Time evolution of the skewness S_u of the longitudinal velocity derivative (left) and of the flatness $F_{\boldsymbol{\omega}}$ of vorticity (right).*

flow in these CVS runs is more intermittent than in the DNS. Although the flatness value for CVS2 is below that for DNS, the moduli of deviations of the flatness values of CVS2 and CVS1 from the DNS value are nearly the same. CVS4 yields much smaller values than the DNS for both the skewness and the flatness.

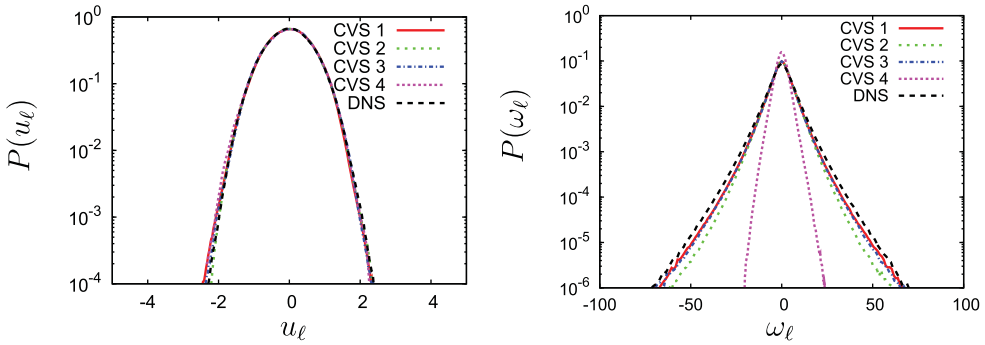

FIG. 4.6. *PDFs of velocity (left) and vorticity (right) at* $t/\tau = 3.78$.

Probability distribution functions (PDFs) of velocity and vorticity are shown in Figure 4.6 for the four CVS runs together with the DNS. The velocity PDFs (Figure 4.6, left) of all the CVS runs agree well with the velocity PDF of the DNS and exhibit a Gaussian shape. For the vorticity PDFs (Figure 4.6, right), this picture differs. For CVS1–3, the PDFs of the coherent vorticity present almost the same stretched exponential shape as that for the DNS. In contrast, the variance for CVS4 is significantly reduced, and hence the heavy tails present in DNS are not reproduced in CVS4.

Thus, we can draw the following conclusions:

(i) CVS1 yields the best results among CVS1–4 but also has the largest number of coefficients.

(ii) CVS2 has the best compression among CVS1–3, while keeping the statistical predictability of the turbulent flow.

(iii) In CVS4, the flow dynamics of DNS has been destroyed.

Finally, we study the difference of the threshold value T_1 when filtering a fully developed turbulent field obtained by DNS at a given time instant with the value of T_1 we obtain during time stepping of CVS. We examine this point by computing two kinds of threshold values: One is obtained by applying the CVE filter to the DNS field at the final time $t = 3.78\tau$. The other is the threshold value used in the CVS computations, again at $t = 3.78\tau$. We call here the former CVE threshold and the latter CVS threshold. For the CVE threshold, we obtain $T_1 = 23.4$, while the CVS thresholds for CVS1–4 are given as 16.4, 13.4, 15.0, and 1.6, respectively. Thus, we find that the threshold values are smaller in the CVS runs, compared to a CVE filtering applied to the DNS data. It is remarkable that the threshold values of CVS, except CVS4 which has no safety zone, are of the same order as those obtained by filtering the DNS result.

4.2. Influence of the threshold. We examine the influence of the threshold value T in (2.2) for the CVS computations with the safety zone in space, scale, and direction. Therefore, we performed another CVS, denoted by CVS0, whose threshold is taken as $T = T_0$, i.e., without any iteration. The threshold value T_0 is larger than T_1 used in CVS1, and therefore CVS0 does retain fewer coefficients than CVS1. Indeed, the percentage of the retained coefficients in CVS0 is about 10% for $t > 0.5\tau$ (figure not shown here), while the percentage in CVS1 is about 30%. Nevertheless CVS0 works well thanks to the addition of the safety zone added to the coherent vorticity, although the coherent vorticity extracted by wavelet filtering with $T = T_0$ does not preserve the statistics of the instantaneous turbulent field as well as with $T = T_1$.

The comparison of CVS0 with CVS1 in Figure 4.7(left) shows that the energy evolution is not very sensitive to the choice of the threshold. In contrast, the enstrophy

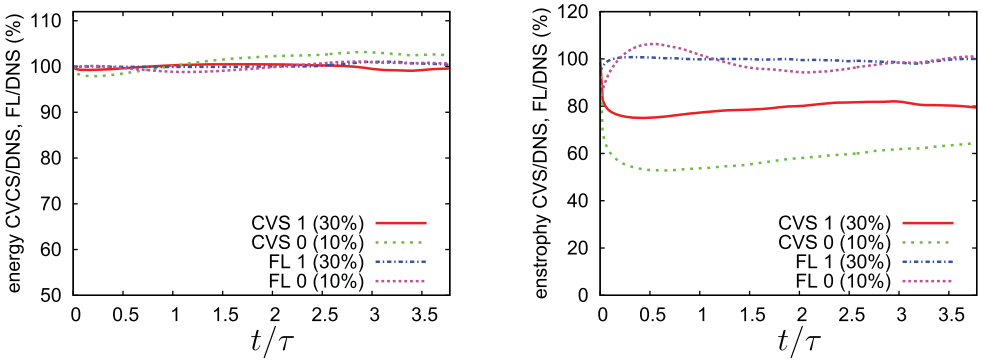

FIG. 4.7. *The energy ratio of CVS/DNS and FL/DNS (left) and the enstrophy ratio of CVS/DNS and FL/DNS (right).*

evolution (Figure 4.7, right) changes significantly. However, this is not a problem as long as energy is conserved. The loss of enstrophy corresponds to the incoherent enstrophy which is removed at each time step by the filtering. CVS1 retains about 80% of the enstrophy, while CVS0 retains about 60% of the enstrophy. Figure 4.8(left) shows that CVS0 has almost the same energy spectrum as the DNS reference in the inertial range. In Figure 4.8(right), the energy flux in CVS0 is in reasonable agreement with that in DNS. CVS0 preserves reasonably well higher order statistics, i.e., skewness and flatness presented in Figure 4.9, of the DNS results. Intense vorticity regions for CVS0 are visualized in Figure 4.2(top, left). CVS0 exhibits entangled vortex tubes similar to the tubes observed in DNS and also well preserved in CVS1–3.

For two-dimensional decaying turbulence, it was verified that CVS using the threshold $T = T_0$ and with the safety zone in space, scale, and direction preserves the statistics of DNS well [25].

4.3. Comparison with Fourier truncated simulation. We compare CVS with Fourier truncated simulation with respect to the statistical predictability of turbulence. Two computations (FL0 and FL1) were performed using the spectral cutoff filter. We do not employ any subgrid-scale model in FL0 and FL1 since the influence of the discarded field onto the resolved field is not modeled for the present CVS computations either. The cutoff wavenumber k_c is chosen such that the percentage of the retained Fourier

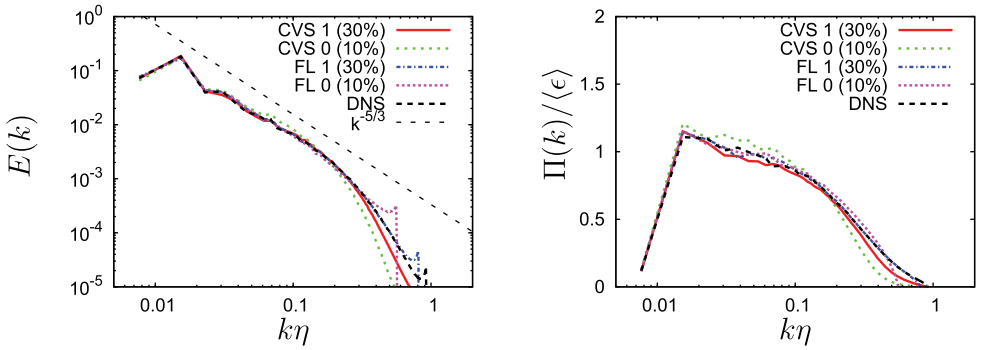

FIG. 4.8. *Energy spectra $E(k)$ (left) and energy fluxes $\Pi(k)$ (right) at $t/\tau = 3.78$. The wavenumber k and the flux $\Pi(k)$ are respectively normalized by η and $\langle\epsilon\rangle$ of the DNS at $t/\tau = 3.78$.*

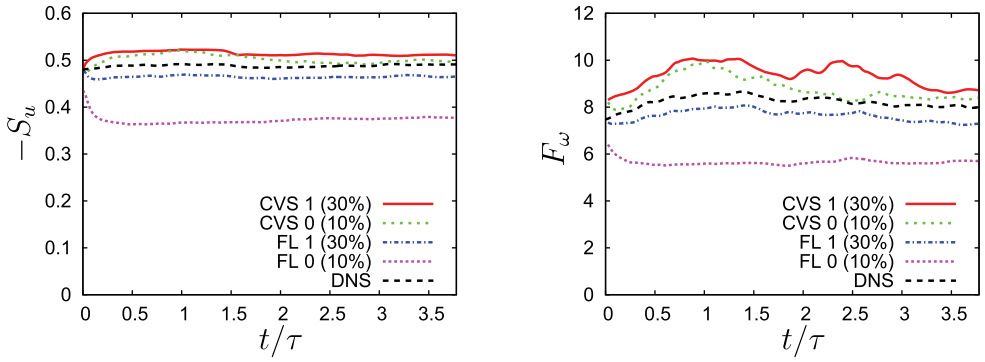

FIG. 4.9. *Time evolution of the skewness S_u of the longitudinal velocity derivative (left) and of the flatness F_ω of vorticity (right).*

coefficients is almost the same as for the retained wavelet coefficients in CVS0 and CVS1, i.e., 10% and 30%, respectively. Note that CVS does not require the addition of a subgrid-scale model, since CVS zeros out the energy that arrives outside of Λ_*.

First, we compare FL0 with CVS0. Figure 4.7(left) shows that both CVS0 and FL0 yield reasonable predictability for the time evolution of energy. The time evolution of the enstrophy ratio, plotted in Figure 4.7(right), is about 100% for FL0, while CVS0 retains about 60% of the enstrophy of DNS for $t > 0.5\tau$. This loss of enstrophy is due to the fact that CVS removes the incoherent enstrophy while retaining the energy, as explained in the previous subsection. In Figure 4.8(left), we see that FL0 tends to pile up energy near the cutoff wavenumber in its energy spectrum, while CVS0 does not. The influence of the pileup on the enstrophy for FL0 can be estimated to be 18%. This percentage is calculated by $100 \times \int_0^{k_c} k^2 E_{\mathrm{FL0}}(k)\mathrm{d}k / \int_0^{k_c} k^2 E_{\mathrm{DNS}}(k)\mathrm{d}k$, where $E_{\mathrm{FL0}}(k)$ and $E_{\mathrm{DNS}}(k)$ are the energy spectra for FL0 and DNS at the final time of the simulations, respectively. The energy fluxes for FL0 and CVS0 are in good agreement with the energy flux of DNS. In Figure 4.9, we see that the skewness and flatness of FL0 are much smaller than those of DNS, while CVS0 preserves the higher order statistics of DNS reasonably well.

Next, we compare FL1 with CVS1. In contrast to the comparison of CVS0 with FL0, there is little difference between the statistical predictability of CVS1 and FL1. Figures 4.7, 4.8, and 4.9 show that FL1 well preserves the DNS results studied here. The statistics of DNS are well predicted by CVS1, as discussed in subsection 4.1.

Therefore, we find that, as the number of the retained coefficients decreases, the wavelet representation is more suitable for predicting the third- and fourth-order turbulence statistics than the Fourier representation.

5. Conclusions and perspectives. CVS computations of three-dimensional forced homogeneous isotropic turbulence have been performed and compared with a reference DNS at initial Taylor microscale Reynolds number $R_\lambda = 153$ and resolution $N = 256^3$. Different strategies for choosing the safety zone and the threshold value have been assessed in terms of statistical predictability and reduction of the number of degrees of freedom to be computed. Three-dimensional homogeneous isotropic turbulence was chosen to demonstrate the feasibility and efficiency of CVS in the most challenging case.

We found that the statistics of the reference DNS are well preserved by CVS if a safety zone is provided in wavelet space. Of course, as any truncated method, CVS cannot preserve the deterministic predictability when the flow has become turbulent (due to the sensitivity to initial conditions). CVS1, which has a safety zone in space, scale, and

direction, presents the best statistical predictability, but the number of computed degrees of freedom is in this case only reduced by a factor of three in comparison to DNS. To improve the computational efficiency of CVS we then proposed two strategies to further reduce the number of degrees of freedom. One is to reduce the safety zone and the other to raise the threshold value. Thus, CVS2 has a reduced safety zone, where neighbor coefficients are only retained in space and direction but not in scale. CVS0 keeps the widest safety zone but increases the threshold value. We found that both methods reduce the number of degrees of freedom by a factor of ten, in comparison to DNS, while preserving an excellent statistical predictability of the turbulent flow evolution. In contrast, the flow dynamics, as well as the flow statistics, are lost for CVS4 which does not have any safety zone. The statistical predictability seems similar for CVS0 and CVS2. However, we conjecture that CVS0 may be better suited for computing the transition between the laminar and the turbulent flow regime than CVS2 since the production of small-scale vortices plays a significant role to trigger this transition. It was shown that information which travels further than the adjacent wavelet coefficients is not crucial to track the evolution of the nonlinear dynamics since all the CVS with safety zone well retain the statistics of DNS. The small divergence contribution in the coherent vorticity field has been confirmed to be not significant.

We have also compared CVS with Fourier truncated simulations, where Fourier coefficients are removed if their wavenumber is larger than a given cutoff value. We did not add any subgrid or other turbulence models to either CVS or Fourier truncated simulations. We found that, as the number of retained coefficients decreases, the wavelet representation better predicts the turbulence statistics, in particular the vorticity PDF, than the Fourier representation.

In contrast to LES, where only the evolution of the large scales is computed, CVS covers the full range of the energy spectrum, even retaining some modes in the dissipative range which still contribute to the nonlinear dynamics. Moreover, CVS does not require the addition of a subgrid-scale model to take into account the effect of the unresolved onto the resolved scales, as necessary for LES. Indeed, neglecting the incoherent modes, whatever their scale, removes the incoherent enstrophy without affecting the energy, which is sufficient to model the turbulent dissipation and efficiently compute the flow evolution in the fully developed turbulent regime.

The presented CVS feasability study deals with homogeneous isotropic turbulence which can be seen as the worst case for CVS. The coherent vortices are distributed statistically homogeneously over the whole flow domain. Inhomogeneous flows allow for higher compression rates. For example, in [24] temporally developing mixing layers have been studied at resolution $N = 128^3$. It was shown that between 9% and 15% of the wavelet modes, depending on the flow evolution, were sufficient to track the dynamics of the flow.

Concerning CVS of flows in complex geometries, we propose to use the volume penalization approach. In [23], two-dimensional flows past an impulsively started cylinder have been computed using an adaptive wavelet method. It was shown that the grid is automatically adapted to both the flow and the geometry. CVS well captures the flow dynamics with 8% of the wavelet coefficients compared to DNS.

In this work, the incoherent vorticity is discarded during the CVS computations. Before modeling the effect of the incoherent field onto the coherent field, a parametric study for different time increments and different numbers of grid points should be performed at the same Reynolds number in order to estimate how the statistical properties of the incoherent vorticity may change.

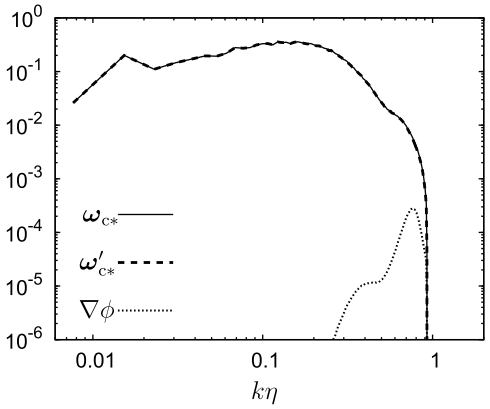

FIG. A.1. *Spectra of the coherent vorticity* $\boldsymbol{\omega}_{c*}$*, its incompressible and compressible contributions,* $\boldsymbol{\omega}'_{c*}$ *and* $\nabla\boldsymbol{\phi}$*, respectively, at* $t = 3.78\tau$.

Appendix A. Divergence issue. We assess the influence of the divergence of the coherent vorticity $\boldsymbol{\omega}_{c*}$ at the final time $t = 3.78\tau$ for CVS2. Figure A.1 shows the spectra of the $\boldsymbol{\omega}_{c*}$, its divergence-free part $\boldsymbol{\omega}'_{c*}$ and its compressible contribution $\nabla\boldsymbol{\phi}$, where $\boldsymbol{\omega}'_{c*} = \boldsymbol{\omega}_{c*} + \nabla\boldsymbol{\phi}$. We observe that the spectrum of $\boldsymbol{\omega}_{c*}$ agrees well with that of $\boldsymbol{\omega}'_{c*}$. The compressible contribution occurs only in the dissipative range and remains several orders of magnitude below the incompressible part. The relative error of the divergence part is estimated by $100 \times \langle|\nabla\boldsymbol{\phi}|^2\rangle / \langle|\boldsymbol{\omega}_{c*}|^2\rangle \sim 5.4 \times 10^{-2}[\%]$. Therefore, the influence of $\nabla\boldsymbol{\phi}$ on $\boldsymbol{\omega}_{c*}$ is negligible in CVS.

Appendix B. Numerical cost of fully adaptive CVS.

B.1. Ideal savings. The ideal savings of CVS with respect to CPU time and memory depend on the size of the safety zone and the choice of the threshold because the savings are directly related to the compression. For example, in CVS0, they would be 90%, as only about 10% of the coefficients are retained.

The incompressibility constraint for the velocity field requires the solution of Poisson equations in each time step. The equations are solved for the "adaptive degrees of freedom", i.e., the retained wavelet coefficients. For this task, an iterative solver could be employed. The wavelet representation yields an easy, i.e., diagonal, preconditioner of the equations with a condition number which is uniformly bounded, as shown in [14]. Therefore, the complexity for solving the linear systems should be of order $O(N_{ad})$, where N_{ad} denotes the number of adaptive degrees of freedom. Preconditioned Krylov space solvers and a geometric multigrid solver allow one to solve the equations; for the latter, its implementation is more sophisticated.

B.2. Actual savings. In the ideal savings, the computation of one adaptive degree of freedom would not be more expensive than one degree of freedom on a regular grid in DNS. For the above example, CVS0, the fully adaptive code would be faster than the DNS code only if the computation of one adaptive degree of freedom is less than 10 times more expensive than that of one degree of freedom in DNS. However, in fully adaptive computations, the computation of one adaptive degree of freedom is typically more expensive than that of one degree of freedom on a regular grid in DNS because there are different types of overhead in the adaptive CVS computations. The overhead consists in the memory access of the data structure required to store the adaptive grid, forward and

backward wavelet transforms, thresholding, and management of the safety zone. A detailed discussion of the overhead comparing a multiresolution scheme with adaptive mesh refinement techniques can be found in [4].

The data structure used to store the adaptive degrees of freedom, which may change over time, requires some additional memory and CPU time for access, compared to the simple sequential arrays used in the DNS code. Typically two options are possible, either a tree data structure, corresponding in three space dimensions to an octree, or a hash table. Due to memory access the tree data structure increases the theoretical complexity of the fully adaptive scheme from $O(N_{ad})$ to $O(N_{ad}\log(N_{ad}))$, while hash tables maintain the theoretical complexity of $O(N_{ad})$.

The discrete wavelet transform is a fast transform algorithm of complexity CN_{ad}, where C is proportional to the filter length of the wavelet. The thresholding iteration also implies some additional CPU time of $O(N_{ad})$, which is, however, negligible as the iteration can be directly performed in wavelet coefficient space. The management of the safety zone also necessitates some additional memory, which is also negligible as only integer values are stored and some CPU time of $O(N_{ad})$.

For weakly compressible mixing layers at maximum resolution $N = 256^3$, Roussel and Schneider [21] found that the CPU time of fully adaptive CVS, which is implemented by using a tree data structure, corresponds to 23.4% of DNS and the memory to 17.1% of DNS. This shows that the computation of one adaptive degree of freedom is 1.38 times more expensive than the computation of one degree of freedom on a regular grid due to the above overheads.

Acknowledgments. The computations were carried out on the Earth Simulator and the FX1 system at the Information Technology Center of Nagoya University. M.F. and K.S. thank the Isaac Newton Institute for Mathematical Sciences, Cambridge for hospitality and financial support during the program on "The Nature of High Reynolds Number Turbulence." M.F. is also thankful to the Wissenschaftskolleg zu Berlin for its hospitality.

REFERENCES

[1] A. Azzalini, M. Farge, and K. Schneider, *Nonlinear wavelet thresholding: A recursive method to determine the optimal denoising threshold*, Appl. Comput. Harmon. Anal., 18 (2005), pp. 177–185.

[2] W. Bos, L. Liechtenstein, and K. Schneider, *Small scale intermittency in anisotropic turbulence.*, Phys. Rev. E, 76 (2007), 046310.

[3] G. Brown and A. Roshko, *On density effects and large structure in turbulent mixing layers*, J. Fluid Mech., 64 (1974), pp. 775–816.

[4] R. Deiterding, M. Domingues, S. Gomes, O. Roussel, and K. Schneider, *Adaptive Multiresolution or Adaptive Mesh Refinement? A Case Study for 2D Euler Equations*, ESAIM Proc. 29, EDP Sci., Les Ulis, 2009, pp. 28–42.

[5] D. Donoho, *De-noising by soft thresholding*, IEEE Trans. Inform. Theory, 41 (1995), pp. 613–627.

[6] M. Farge, *Wavelet transforms and their applications to turbulence*, Annu. Rev. Fluid Mech., 24 (1992), pp. 395–457.

[7] M. Farge, K. Schneider, and N. Kevlahan, *Non-Gaussianity and coherent vortex simulation for two-dimensional turbulence using an adaptive orthonormal wavelet basis*, Phys. Fluids, 11 (1999), pp. 2187–2201.

[8] M. Farge and K. Schneider, *Coherent Vortex Simulation (CVS), a semi-deterministic turbulence model using wavelets*, Flow Turbul. Combust., 66 (2001), pp. 393–426.

[9] M. Farge, G. Pellegrino, and K. Schneider, *Coherent vortex extraction in 3d turbulent flows using orthogonal wavelets*, Phys. Rev. Lett., 87 (2001) pp. 45011–45014.

[10] M. Farge, K. Schneider, G. Pellegrino, A. Wray, and R. Rogallo, *Coherent vortex extraction in three-dimensional homogeneous turbulence: Comparison between CVS-wavelet and POD-Fourier decompositions.*, Phys. Fluids, 15 (2003), pp. 2886–2896.

[11] M. Farge and K. Schneider, *Wavelets: Applications to turbulence*, in Encyclopedia of Mathematical Physics, J.-P. Françoise, G. Naber, and T. S. Tsun, eds., Elsevier, Amsterdam, 2006, pp. 408–419.

[12] J. Fröhlich and K. Schneider, *Computation of decaying turbulence in an adaptive wavelet basis*, Phys. D, 134 (1999), pp. 337–361.

[13] D. Goldstein, O. Vasilyev, and N. Kevlahan, *CVS and SCALES simulation of* 3*-D isotropic turbulence*, J. Turbul., 6 (2005), pp. 1–20.

[14] S. Jaffard, *Wavelet methods for fast resolution of elliptic problems*, SIAM J. Numer. Anal., 29 (1992), pp. 965–986.

[15] M. Lesieur and O. Métais, *New trends in large-eddy simulations of turbulence*, Annu. Rev. Fluid Mech., 28 (1996), pp. 45–82.

[16] S. Mallat, *A Wavelet Tour of Signal Processing, The Sparse Way*, 3rd ed., Elsevier/Academic Press, Amsterdam, 2009.

[17] C. Meneveau, *Analysis of turbulence in the orthonormal wavelet representation*, J. Fluid Mech., 232 (1991), pp. 469–520.

[18] C. Meneveau and J. Katz, *Scale-invariance and turbulence models for large-eddy simulation*, Annu. Rev. Fluid Mech., 32 (2000), pp. 1–32.

[19] Y. Meyer, *Wavelets and Operators*, Cambridge Stud. Adv. Math. 37, Cambridge University Press, Cambridge, UK, 1992.

[20] N. Okamoto, K. Yoshimatsu, K. Schneider, M. Farge, and Y. Kaneda, *Coherent vortices in high resolution direct numerical simulation of homogeneous isotropic turbulence : A wavelet viewpoint*, Phys. Fluids, 19 (2007), 115109.

[21] O. Roussel and K. Schneider, *Coherent Vortex Simulation of weakly compressible turbulent mixing layers using adaptive multiresolution methods*, J. Comput. Phys., 229 (2010), pp. 2267–2286.

[22] P. Sagaut, S. Deck, and M. Terracol, *Multiscale and Multiresolution Approaches in Turbulence*, Imperial College Press, London, 2006.

[23] K. Schneider and M. Farge, *Adaptive wavelet simulation of a flow around an impulsively started cylinder using penalisation*, Appl. Comput. Harmon. Anal., 12 (2002), pp. 374–380.

[24] K. Schneider, M. Farge, G. Pellegrino, and M. Rogers, *Coherent vortex simulation of* 3*D turbulent mixing layers using orthogonal wavelets*, J. Fluid Mech., 534 (2005), pp. 39–66.

[25] K. Schneider, M. Farge, A. Azzalini, and J. Ziuber, *Coherent vortex extraction and simulation of* 2*d isotropic turbulence*, J. Turbul., 7 (2006), pp. 1–24.

[26] K. Schneider and O. Vasilyev, *Wavelet methods in computational fluid dynamics*, Annu. Rev. Fluid Mech., 42 (2010), pp. 473–503.

[27] G. Stefano and O. Vasilyev, *Stochastic coherent adaptive large eddy simulation of forced isotropic turbulence*, J. Fluid Mech., 646 (2010), pp. 453–470.

[28] Y. Yamazaki, T. Ishihara, and Y. Kaneda, *Effect of wavenumber truncation on high-resolution direct numerical simulation of turbulence*, J. Phys. Soc. Japan, 71 (2002), pp. 777–781.

[29] K. Yoshida and T. Arimitsu, *Inertial-subrange structures of isotropic incompressible magnetohydrodynamic turbulence in the Lagrangian renormalized approximation*, Phys. Fluids, 19 (2007), 045106.

[30] K. Yoshimatsu, Y. Kondo, K. Schneider, N. Okamoto, H. Hagiwara, and M. Farge, *Wavelet-based coherent vorticity sheet and current sheet extraction from three-dimensional homogeneous magnetohydrodynamic turbulence*, Phys. Plasmas, 16 (2009), 082306.